DOI: 10.13009/EUCASS2019-516

Experimental Flow Path Analysis of a Hydrogen Transpiration Cooled Model Scramjet Combustor

Friedolin Strauss, Stephan General*, Chiara Manfletti** and Stefan Schlechtriem**

** German Aerospace Center (DLR), Institute of Space Propulsion*
Langer Grund, D-74239 Hardthausen, Germany; friedolin.strauss@dlr.de
*** European Space Agency (ESA), Headquarters*
8-10 rue Mario Nikis, 75738 Paris Cedex 15, France; chiara.manfletti@esa.int

Abstract

Cooling experiments are performed by DLR Institute of Space Propulsion, applying a transpiration cooling system to a scramjet model combustion chamber. Hydrogen coolant is injected through different porous wall samples made of sintered stainless steel into a Mach 2.5 hot gas main flow. Different inlet conditions as well as the response of the transpiration cooling to a shock impingement caused by a 9.3° half wedge at different lateral positions are investigated. Results show good transpiration cooling efficiency which is governed by the impinging shock and its position. Limitations of this cooling approach are also discussed.

Nomenclature

Ma	Mach Number [-]	θ	Cooling Efficiency [-]
T	Temperature [K]	*e*	*Nozzle Exit*
$\dot{m}$	Mass Flow [kg/s]	*c*	*Coolant*
κ	Ratio of Specific Heats [-]	*g*	*Main Flow (Hot Gas)*
Pr	Prandtl Number [-]	*r*	*Recovery*
F	Blowing Ratio [-]	*w*	*Wall*
A	Area [m²]	*turb*	*Turbulent*

1. Introduction

A worldwide demand to replace toxic or hazardous propellants in space flight and international security challenges have brought high-speed air breathing propulsion systems such as supersonic combustion ramjets (so called scramjets) back into focus (see e.g. [1],[2],[3],[4]). Apart from fuel residence time, mixing and controlled ignition, the main challenge is the handling of thermal loads resulting from high-speed flight (around 3000 K wall temperature and 5 MW/m² at Mach 8, see [5]) and supersonic combustion. A promising approach for a cooling system, which could be able to handle those loads is the so-called transpiration cooling. In transpiration cooling systems cold coolant enters the hot gas main flow through a porous wall or porous section (see [6]). The coolant flow provides direct cooling through the porous wall section and additionally to the wall downstream by adding a homogenous and protective coolant film layer close-by. However, the introduction of a coolant secondary flow can lead to shock-boundary layer interaction (see [7]), a choking of the flow in the combustion chamber or, if propellant is used for cooling, boundary layer combustion.

The Institute of Space Propulsion of the German Aerospace Center (DLR) has set up a research test bench equipped with a scramjet model combustion chamber to investigate the applicability of transpiration cooling systems to high-speed air breathing propulsion systems and to examine the resulting phenomena connected with the introduction of a coolant secondary flow into a supersonic hot gas main flow. The observed phenomena and findings can also be applied to other applications of a transpiration cooling system or to similar boundary conditions like in transpiration cooled nozzle extensions of liquid chemical rocket propulsion systems (see [6] and [8]).

Experiments in the past concerning the application of porous media with perfusion in scramjets focused mainly on improvements in the field of mixing and combustion (see [9]), boundary layer control, (e.g. refer to [10]) and external transpiration cooling for high speed flight (see [11]). Numerical work connected with validation experiments

DOI: 10.13009/EUCASS2019-516

focusing on porous media flow properties and cooling applications of hydrocarbon fuel in scramjets has been published by several authors, e.g. in Europe of PRISME / INSA (see [12], [13], [14], [15], [16]). The applicability of transpiration cooling systems in the internal flow path of ramjets and scramjets with CMC ceramics as porous media were investigated by [5]. Heat transfer in the material was numerically and experimentally by [17] and [18].
Recently sintered metals were investigated for application in porous struts for fuel injection in scramjets (see [19] and [20]). Reference [19] performed an experimental and numerical analysis of a strut made of a sintered stainless steel alloy similar to the properties of Sika-R 25 in a Mach 2.5 supersonic flow (same Mach number as in the publication at hand). The stagnation temperature reached in [19] was 1920 K and therefore higher than in the current publication. Gaseous methane was used as a non-inert coolant and injected at a pressure of 4 MPa through a strut into a model combustion chamber with a 50x70 mm cross section (cross section area ca. 40% larger than in the current publication).
Reference [20] performed experiments on combined transpiration and film cooling with a symmetrical wedge-shaped strut with about a 7° half angle made of an alloy similar to [19], and therefore similar to Sika-R 25. The Mach number of the main flow was 2.8, stagnation temperature was 398.15 K and the stagnation pressure was 4.8 bar. Hot gas mass flow could be back-calculated by the authors of the current publication to about 0.4 kg/s through a 20x30 mm cross section (ca. 30% of the cross section used in this publication). Work on the effects of shock generators has also been published by [21] for 2D shock generators with 10 / 15 / 20° turning angles. The oblique shocks impinged downstream of a series of holes equipped with small nozzles (wall jets). Reference [21] introduced a Mach 3.0 helium secondary flow through those holes into a Mach 6.4 main flow with a short test duration of 25 ms. The work of reference [21] was followed by the experiments of [22], which investigated a transpiration-cooled surface made of composite sandwich material. In [22] shocks at turning angles of 5 / 7.5 / 10° were impinged on the transpiration cooled surface at free stream Mach numbers of 6.4 and 7.9. These represent the highest Mach numbers that would be developed in a scramjet combustor. Inert coolants were used for cooling (gaseous nitrogen and helium) at different blowing ratios. Reference [23] completed this analysis as a follow-up with experiments on shock-boundary layer interaction, but with a film cooling system instead. Their shock generator, with 2 / 5 / 7.5° turning angles, induced an impinging swept-shock downstream of a film cooling slot. The coolants used were helium and hydrogen, entering the Mach 6.4 nitrogen inert free stream at Mach numbers of 2.7 (hydrogen) and 3.0 (helium). Interaction with a reflected expansion was also investigated.
Several other publications used sintered metals to create transpiration cooling systems similar to the porous samples investigated in the current publication. Reference [24] investigated the effect of foreign gas transpiration into a turbulent boundary layer at Mach numbers smaller than 0.35 and a main flow with a stagnation temperature between 298 K and 563 K at a mass flow of 1.3 kg/s. The coolants used were air, nitrogen, helium, and argon through porous samples with porosities of 20% and 30% (similar to Sika-R 0.5 and Sika-R 5). Reference [25] experimented with a transpiration cooling system under laboratory conditions without hot gas main flow. The authors simulated the heat flux by arc lamps, which heat up porous tubes made of stainless steel and Inconel. This setup created temperatures up to 1373 K at the specimen. Pore diameters of 1.5, 3, and 5 µm were similar to Sika-R 1.5, Sika-R 3, and Sika-R 5. Experimental and numerical investigations on transpiration cooling for sintered porous flat plates has also been performed by [26] using material similar to Sika-B 40 / Sika-B 90 (bronze) and Sika-R 40 / Sika-R 90 (stainless steel) in a low-temperature, low speed main flow of 373 K stagnation temperature and 30 m/s flow velocity. This investigation was extended by [27] for transpiration cooling systems with phase change using water as coolant into a 800 K stagnation temperature main flow of 65 m/s. The channel's cross section was 50x80 mm and the geometry of the porous plates was 80x40 mm.
Several publications can be found on film cooling, using either similar experimental conditions or similar porous media with the same coolants as the current publication. Reference [28] injected coolant at a Mach number of 3.0 into a Mach 6.4 1181 K main flow, using helium as coolant. Incident shocks were created by a 0 / 5 / 10° turning-angle ramp. A very thorough analysis of air and hydrogen at different blowing ratios into a Mach 6 main flow has been published by [29]. Reference [29] used helium coolant entering a Mach 6 main flow at a rearward facing step with a 10° turning angle shock generator present. Downstream effects of a transpiration cooling system in an air and helium transpiration cooled nozzle were analyzed by [30].
DLR investigated the transpiration cooling in a scramjet model combustion chamber for inert coolants (gaseous nitrogen), using the boundary conditions presented in section 4 of the current publication (see also [31] and [32] for details) as well as with reactive hydrogen (see [33] and [34]). Furthermore, boundary layer combustion, in this case for internal drag reduction, has been addressed by [35].

DOI: 10.13009/EUCASS2019-516

2. Test Setup

The main flow test conditions for the experiment are provided by a chemical air vitiator (see [31] and [36] for design details and a performance analysis of the boundary conditions provided), which heats up pressurized air by combustion of hydrogen and oxygen. It can achieve a maximum stagnation temperature of 1500 K, a stagnation pressure of up to 25 bar, and a 5 kg/s hot gas mass flow rate.

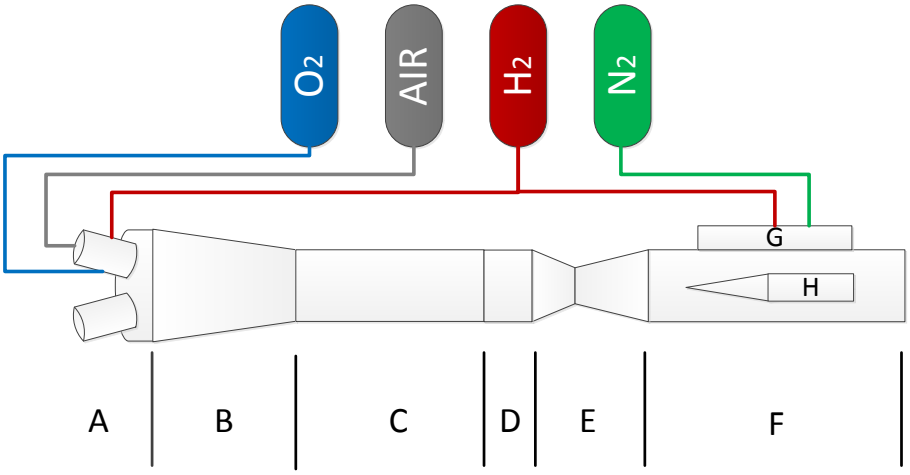

Figure 1: Test Bench Scheme

The air vitiator is controlled by a Siemens® Simatic 7 SPS control system, which monitors red line definitions, the selected pre-pressures for the supplies, and the test run sequences. The hydrogen/oxygen burners ("A" in Fig. 1) can be selected in groups from 1 to all 11 burners, and feature exchangeable sonic orifices in their burner heads to further adjust them to the needs of the experimental main flow test conditions.
A geometrical transition section ("D" in Fig. 1 and [31], [36] for details) is connected to the air vitiator ("A", "B" and "C" in Fig. 1) changing the cross section from 135 mm diameter to 45 x 45 mm square. The transition section is followed by a Mach 2.5 supersonic nozzle downstream ("E" in Fig. 1), which is connected to a 300 mm long scramjet model combustor ("F" in Fig. 1) with an internal cross section of 45 x 45 mm square. This model combustion chamber is equipped with a porous wall section (100 x 30 mm, maximum thickness 20 mm) at the upper wall, which is supplied with coolant (gaseous hydrogen or gaseous nitrogen) by a plenum ("G" in Fig. 1). A flow deflector integrated into the plenum ensures a homogeneous coolant distribution to the porous sample. Two quartz glass windows provide lateral optical access to the flow path. An optional wedge-shaped shock generator ("H" in Fig. 1, length 80 mm, width 44 mm, 9.3° ramp angle) can be added to the model combustion chamber. The shock generator can be freely positioned in the horizontal plane of the lower wall by a pressure tight positioning mechanism.

3. Measurement and Data Acquisitioning Equipment

The intrusive pressure and temperature measurement equipment consists of two groups of sensors: First, a permanent part, which is included in the model combustion chamber and the air vitiator's measurement section. Second a non-permanent part, which is mounted to the model combustion chamber by the use of optional measurement plates, which are inserted either into cut-outs in the lower wall instead of the shock generator, or to replace one of the lateral quartz glass windows, depending on the test configuration used. Those measurement plates feature additional pressure and temperature sensors (see [31]).
The temperature measurement array included in the basic measurement equipment consists of eight thermocouples (*Thermosensors Type K*, "ST-01" to "ST-08" in Fig. 2) in two rows with four sensors each in a distance of 7.50 mm to the channel's middle axis at the upper wall. They are measuring the coolant wake region 26 mm to 56 mm downstream of the porous sample (see Fig. 2). Additionally, three static pressure ports located on axis and equipped with pressure sensors (*Measurement Specialities Type P913-G003, 0-10 bar abs.*, "SP-01" to "SP-03" in Fig. 2) detect the pressure distribution in this area. Static pressure and temperature at the inlet plane are determined by a pressure transducer (*Kistler 4043A20, 0-20 bar abs.*, "SP-IN" in Fig. 2) and a thermocouple (*Thermosensors Type K*, "ST-IN" in Fig. 2). Four static pressure transducers (2x *Kistler 4045A50, 0-50 bar abs.* and 2x *Kistler 2043A20, 0-20 bar abs.*, "SP-PL1" to "SP-PL4" in Fig. 2) and a thermocouple (*Thermosensors Type K*, "ST-PL" in Fig. 2) determine the properties of the coolant right before entering the porous wall slab and ensure the detection of any

DOI: 10.13009/EUCASS2019-516

inhomogeneity in the coolant flow distribution. Coolant mass flow rate is measured by a Coriolis mass flow meter (*Micro Motion ELITE CMF010M*). For the sensor positions of the non-permanent part, that covers the additional measurement plates, see also reference [31].

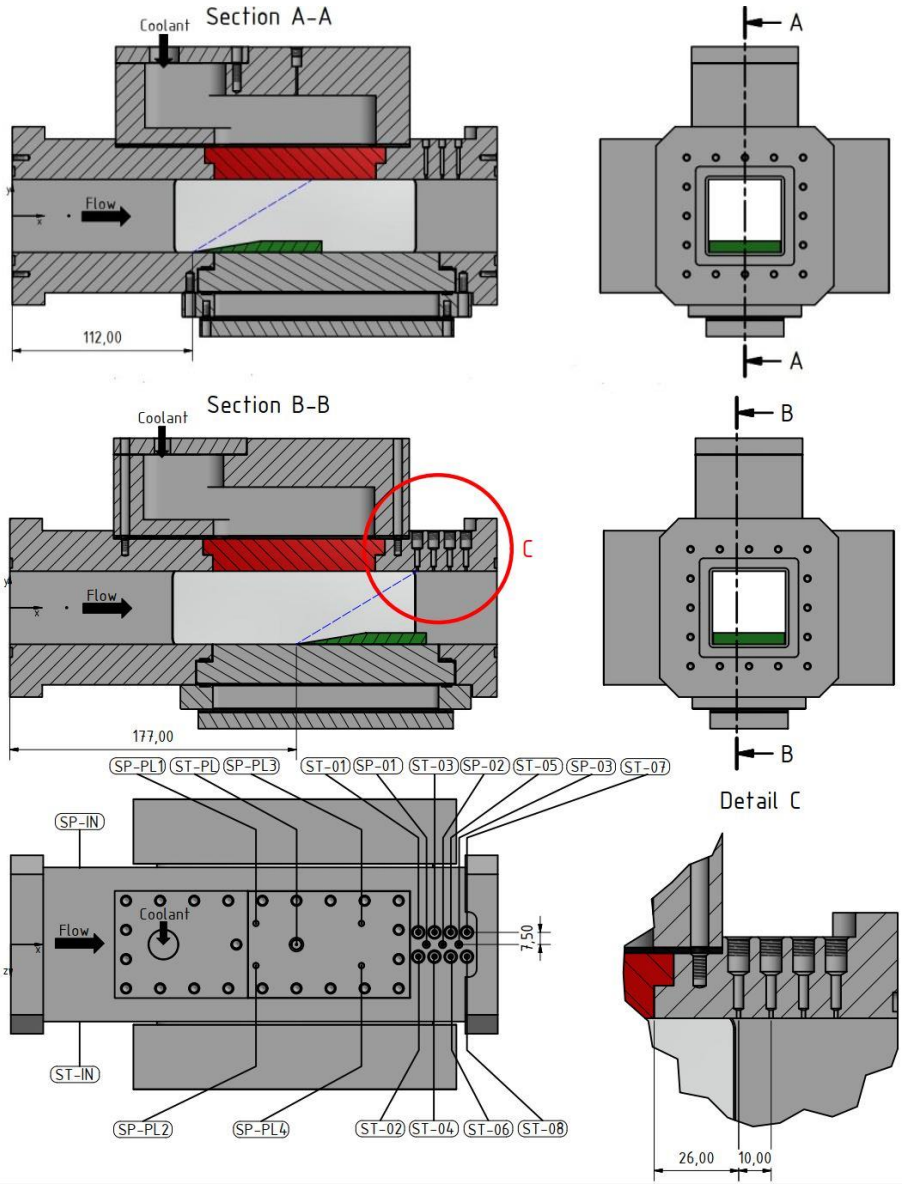

Figure 2: Basic Measurement Equipment Sensor Positions for both Shock Generator Positions

Complimentary to the intrusive measurement equipment, the test rig is equipped with an optical bench in Toepler's Z-type configuration (see [37] for details). Its total length is 7.0 m with a measuring section length of 1.0 m. Two *f*/10 mirrors with 150 mm diameter are used to fold the beam path. This setup can either accommodate a classic schlieren system with a bright light source (Cree LED with a power of 3 W and a 8000 K colour temperature) and a CCD camera (*The Imagine Source DFK 33 GX174e*, 1920 x 1200 p, 2.3 MP, 50 fps), or a Background Oriented Schlieren (BOS) (see [38] for details) system with a 1200 dpi speckle background pattern, an ultra-bright light source (22 Cree® XP-E2-Q4 green high power LEDs) and an industrial CCD camera (FLIR® Blackfly® S BFS-U3-51S5M-C, 200 fps), equipped with a C-mount lens (Fujinon® HF50HA-1B, 1:2,3/50 mm). The field of view of both systems covers the complete area of the lateral windows. The BOS system was shown during experimentation to be less affected by the changes in the refractive index of the quartz glass windows due to strong heating

Data acquisition (DAQ) is provided by a *Werum 2 DAQ* system, featuring 20 HF channels for the pressure sensors and 24 LF channels for the thermocouples. HF channels are sampled at a rate of 20 kHz, whereas LF channels are sampled at 5 kHz. All thermocouples are temperature compensated by an ice box. All pressure sensors were calibrated against ambient pressure prior to each test run.

DOI: 10.13009/EUCASS2019-516

4. Experimental Methodology

Every main flow test condition of the air vitiator (see Table 1) was tested with three different testing configurations. In configuration 1 a blank insert with additional measurement equipment is placed in the model combustion chamber's bottom cutout instead of the shock generator. Optical access for schlieren or BOS imagery is provided by lateral windows. In configuration 2 the measurement plate is replaced with a shock generator. Configuration 3 provides no optical access for schlieren or BOS, but features a lateral blank insert with additional measurement equipment. See [31] and [32] for details on the different testing configurations and Table 2 for an overview.

Table 1: Air Vitiator Main Flow Test Conditions

Stagnation Temperature Preset [K]	**Stagnation Pressure Preset [bar]**	**Total Mass Flow Preset [kg/s]**	**Main Flow Reynolds Number at Channel Intake Plane [-]**
900	10.0	0.905	7.95×10^5
900	15.0	1.358	11.60×10^5
1200	10.0	0.784	5.88×10^5
1200	15.0	1.135	8.40×10^5

Table 2: Test Configurations and Measurement Equipment

Shock Generator Position (from inlet plane)	**112 mm**			**177 mm**	
Test Configuration	**Config. 1**	**Config. 2**	**Config. 3**	**Config. 1**	**Config. 2**
Basic Measurement Equipment	Yes	Yes	Yes	Yes	Yes
Measurement Plate Bottom Wall	Yes	No	No	Yes	No
Measurement Plate Side Wall	No	No	Yes	No	No
Schlieren	Yes	Yes	No	Yes	Yes
Background Oriented Schlieren (BOS)	Yes	Yes	No	Yes	Yes
Shock Generator	No	Yes	Yes	No	Yes

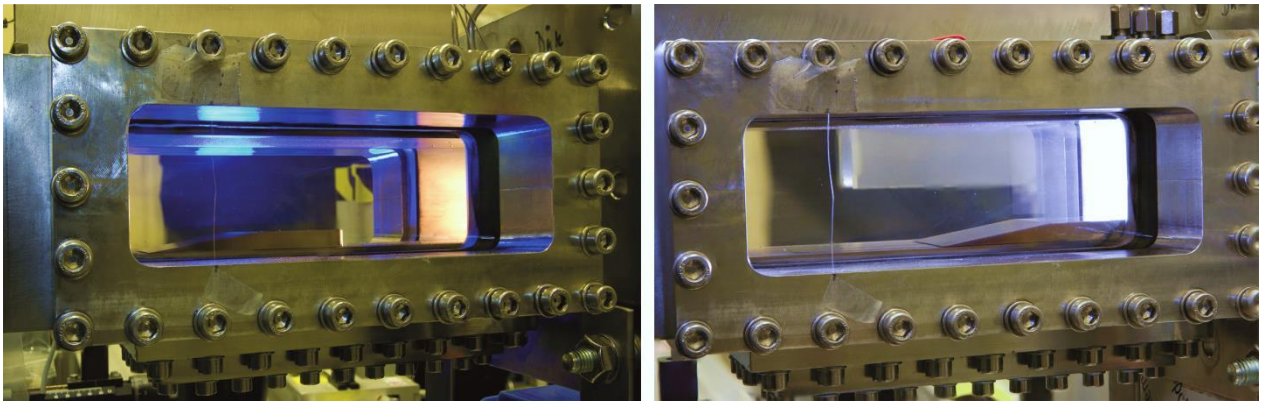

Figure 3: Model Combustion Chamber with Shock Generator at Position 112 mm (left) and 177 mm (right)

DOI: 10.13009/EUCASS2019-516

Table 3: Material Properties of Porous Media Used in the Tests

	Sika-R 150	**Sika-IL 20**	**Sika-IL 1**
Mean Pore Diameter [µm]	150	20	1
Porosity [%] according to DIN EN ISO 2738	48	43	24
Thickness [mm]	20	20	20
Material	1.4404	Inconel® 600	Inconel® 600

Table 4: Coolant Plenum Pressure Presets and Resulting Plenum Pressures

Porous Material	**Coolant**	**Coolant Pressure Preset [bar]**	**Resulting Coolant Plenum Pressure [bar]**
Sika-R150	Nitrogen	0.0	0.0
		50.0	approx. 3.0
		100.0	approx. 5.8
		120.0	approx. 7.2
	Hydrogen	0.0	0.0
		45.0	approx. 3.0
		95.0	approx. 5.8
		120.0	approx. 7.2
Sika-IL20	Nitrogen	0.0	0.0
		30.0	approx. 3.9
		50.0	approx. 6.0
		65.0	approx. 7.5
	Hydrogen	0.0	0.0
		25.0	approx. 3.9
		45.0	approx. 6.0
		60.0	approx. 7.5
Sika-IL1	Nitrogen	0.0	0.0
		5.0	approx. 5.0
		15.0	approx. 13.5
		20.0	approx. 18.0
	Hydrogen	0.0	0.0
		5.0	approx. 5.0
		14.0	approx. 13.5
		19.0	approx. 18.0

Three different porous materials were used (see Table 3 and [31], [32] for details). Four different coolant pre-pressures in the coolant plenum were selected at each testing point (see Table 4 and [31], [32] for details) and for each of the two coolants. For the publication at hand two different lateral positions of the shock generator were investigated in configuration 1 and 2. The upstream position (112 mm from the channel's inlet plane) forces the oblique shock, caused by the shock generator, to impinge on the porous surface at about 2/3 of its length (see blue dashed line in Fig. 2 and Fig. 3). Optical flow investigation indicates that in the case of a coolant boundary layer separation, the reattachment takes place before the boundary layer reaches the temperature measurement array. The second shock generator position at 177 mm shifts the impingement point to a position just upstream of the

DOI: 10.13009/EUCASS2019-516

thermocouple array (see Fig. 2). This also shifts a possible separation bubble to the area of the array. The difference between coolant preset pressure and resulting plenum pressure in Table 4 is caused by construction-conditioned pressure losses in the supply pipework and valves of the test facility. The typical test duration is 10 s.

5. Results

5.1 Mean Wall Temperature Comparison and Selected Flow Phenomena

In the following paragraph two different shock generator positions 112 mm versus 177 mm are compared for hydrogen coolant and the influence of the shock generator's position is discussed. For a detailed mean wall temperature comparison of nitrogen versus hydrogen and no shock generator versus shock generator refer to [Strauss 2017a and 2017b]. Figure 4 displays the mean wall temperature distribution averaged over thermocouples "ST-01" to "ST-08" (see section 3) for a shock generator position at 112 mm and 900 K, 10 bar stagnation values. Deviations between the uncooled cases are caused by different ambient conditions during the respective test runs. Figure 4 shows that very low blowing ratios of about 0.05 % can have a negative effect on the coolant boundary layer and even increase the mean wall temperature. This effect has also been observed with nitrogen and Sika-IL1 (refer to [31] and [32]). The blowing ratio F is defined according to Eq. (1) and reference [5].

$$F = \frac{\dot{m}_c A_g}{\dot{m}_g A_c} \tag{1}$$

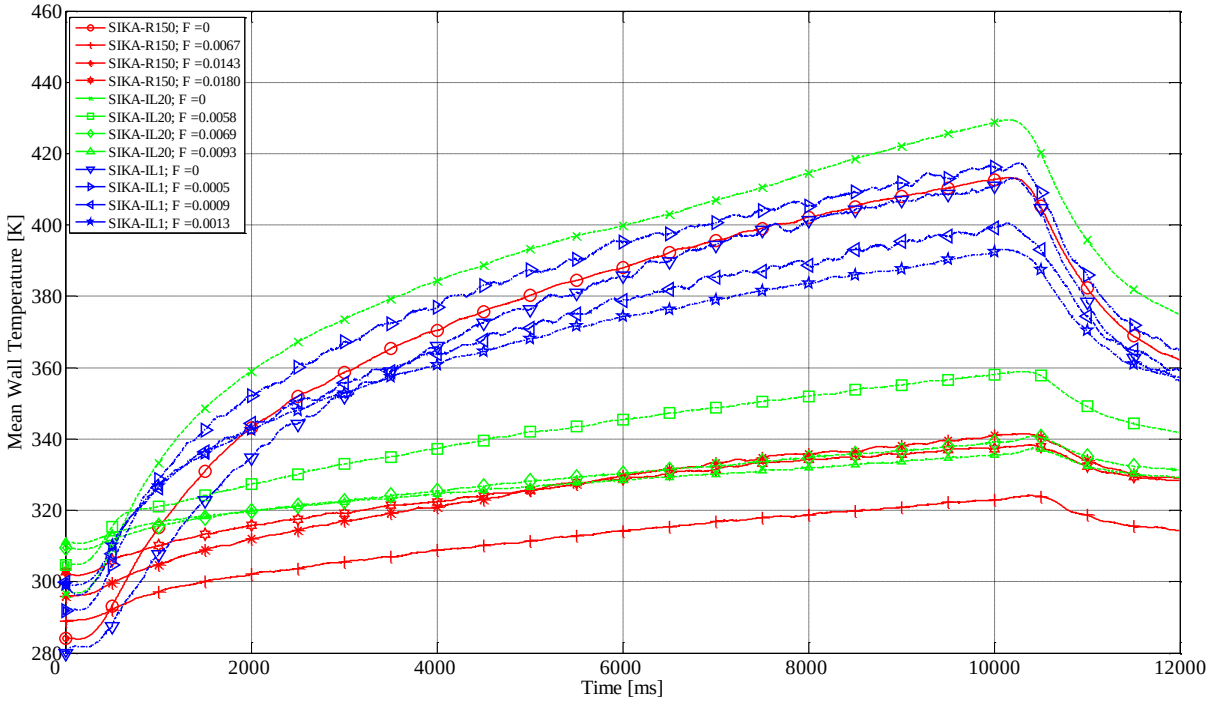

Figure 4: Mean Wall Temperature, 900 K, 10 bar, Hydrogen, Shock Generator Position 112 mm

Due to the thermodynamic properties of hydrogen, already small blowing ratios (refer to Eq. (1)) of about 0.1 % show a significant effect on the wall temperature in the wake region. It can also be shown that there is a kind of saturation point, from which point an increase in blowing ratio results only in a small decrease of the wall temperatures.

In contrast to Fig. 4, Fig. 5 shows the mean wall temperature development with the shock generator positioned at 177 mm. Since the shock now impinges the coolant boundary layer close to the thermocouple array, the mean wall temperature in the uncooled case is about 20 to 30 K higher than in the 112 mm case. Furthermore, the same blowing ratios as in the 112 mm case show less cooling effect in the 177 mm case.

In Fig. 5 the minimal mean wall temperature is achieved in quasi steady-state flow at a 1.77 % blowing ratio and 380 K wall temperature, compared to 320 K at 1.43 % in Fig. 4. In Fig. 5 a sudden rise in the wall temperature is visible after ca 5.5 s testing time and 1.41 % blowing ratio. This is caused by a shock-boundary layer induced auto-ignition of the hydrogen coolant boundary layer. Figure 6 displays the mean wall temperature distribution for a shock

DOI: 10.13009/EUCASS2019-516

generator position at 112 mm at 900 K, 15 bar stagnation values. Caused by the different air vitiator boundary conditions, the shock impingement point on the coolant boundary layer shifts downstream. This leads to a higher mean wall temperature in the uncooled cases compared to Fig. 4 of about 40 K. The mentioned effects of a boundary layer disturbance and an increase of the wall temperature by small blowing ratios are also visible for 112 mm in Fig. 6 and for 177 mm in Fig. 7. The difference between the maximum mean wall temperatures between the 112 mm and 177 mm case can again be determined to about 20-30 K (Fig. 6 compared to Fig. 7).

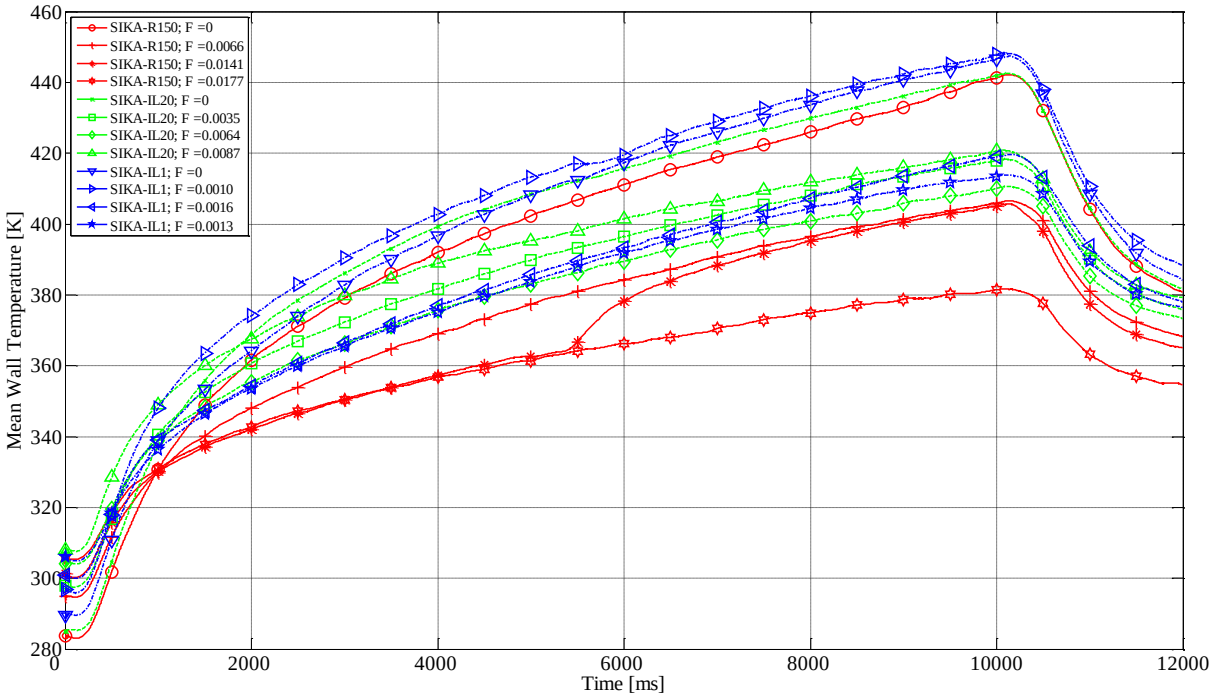

Figure 5: Mean Wall Temperature, 900 K, 10 bar, Hydrogen, Shock Generator Position 177 mm

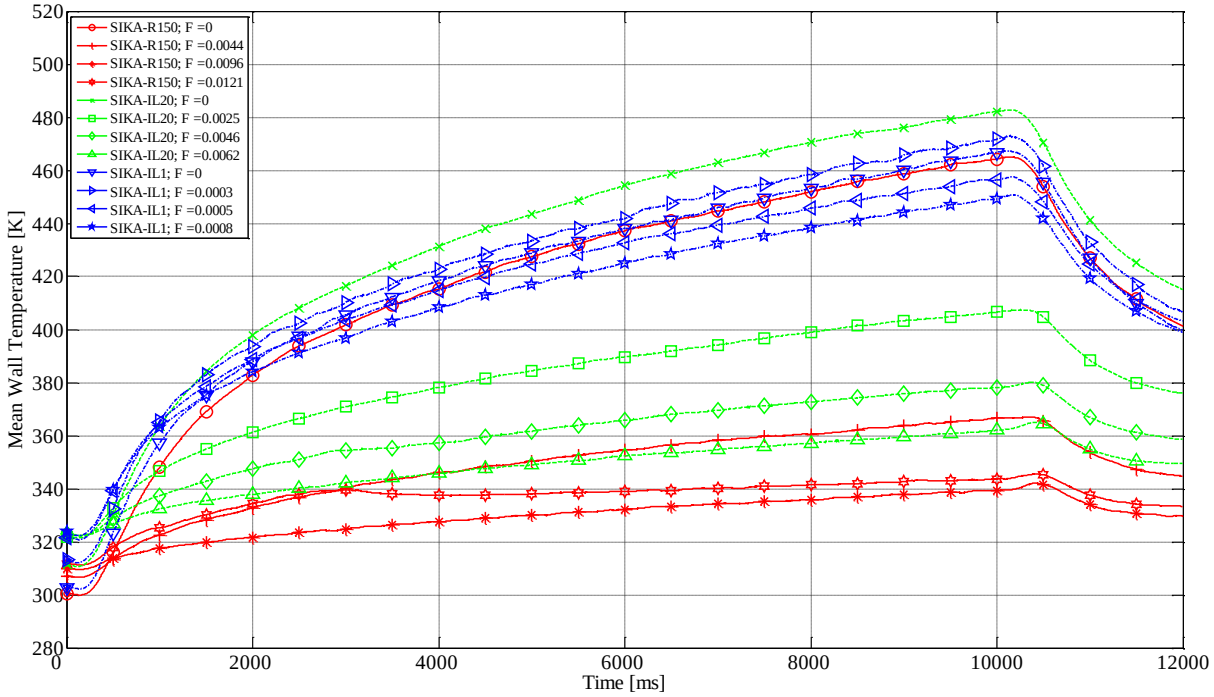

Figure 6: Mean Wall Temperature, 900 K, 15 bar, Hydrogen, Shock Generator Position 112 mm

At a maximum blowing ratio of about 0.96 % the minimum mean wall temperature constitutes 340 K, whereas with the shock generator positioned at 177 mm, the minimum wall temperature of 425 K is reached at a blowing ratio of

DOI: 10.13009/EUCASS2019-516

0.2 %. The graphs in Fig. 6 show that a further increase of the coolant mass flow rate (to 1.21%) leads to an increased mean wall temperature downstream of the porous sample. This phenomenon is caused by a fluctuating shock train, which appears from the start of the flow after ignition of the air vitiator and switches to a normal flow pattern with oblique shocks and expansions but without a shock train after about 3 s. If the shock generator is shifted downstream to its 177 mm position (refer to Fig. 7), this behavior can also be observed at a lower blowing ratio of 0.23 % blowing ratio (Sika-IL20) and 0.43 %.

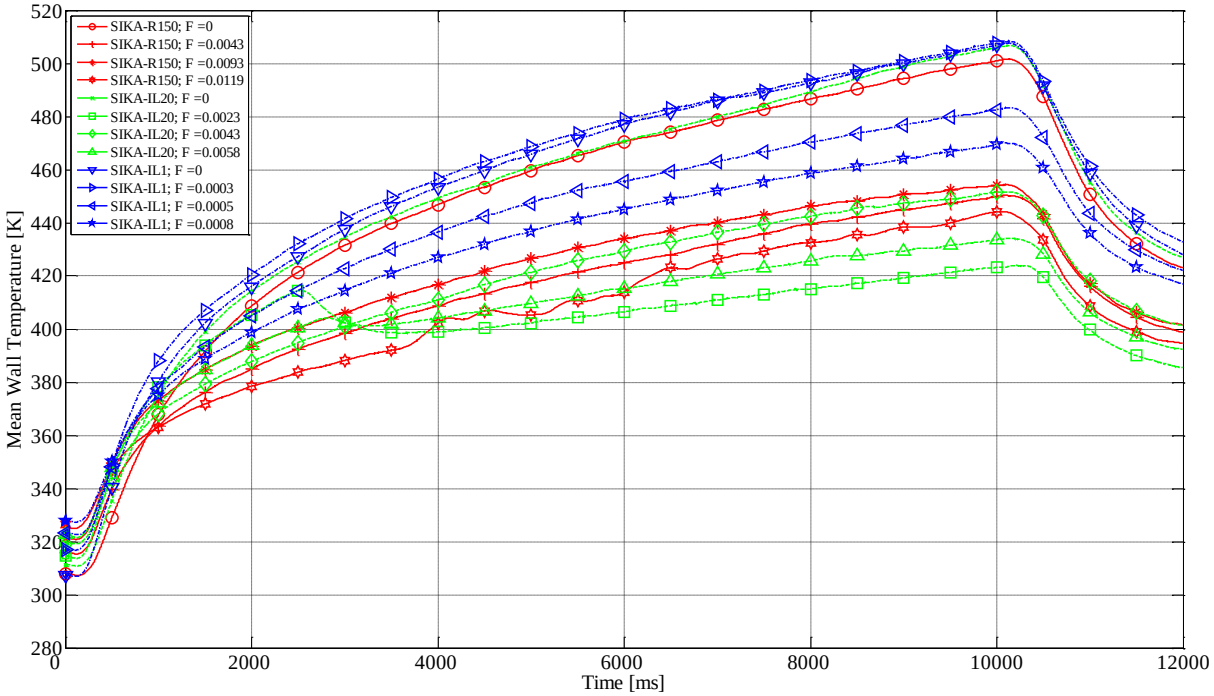

Figure 7: Mean Wall Temperature, 900 K, 15 bar, Hydrogen, Shock Generator Position 177 mm

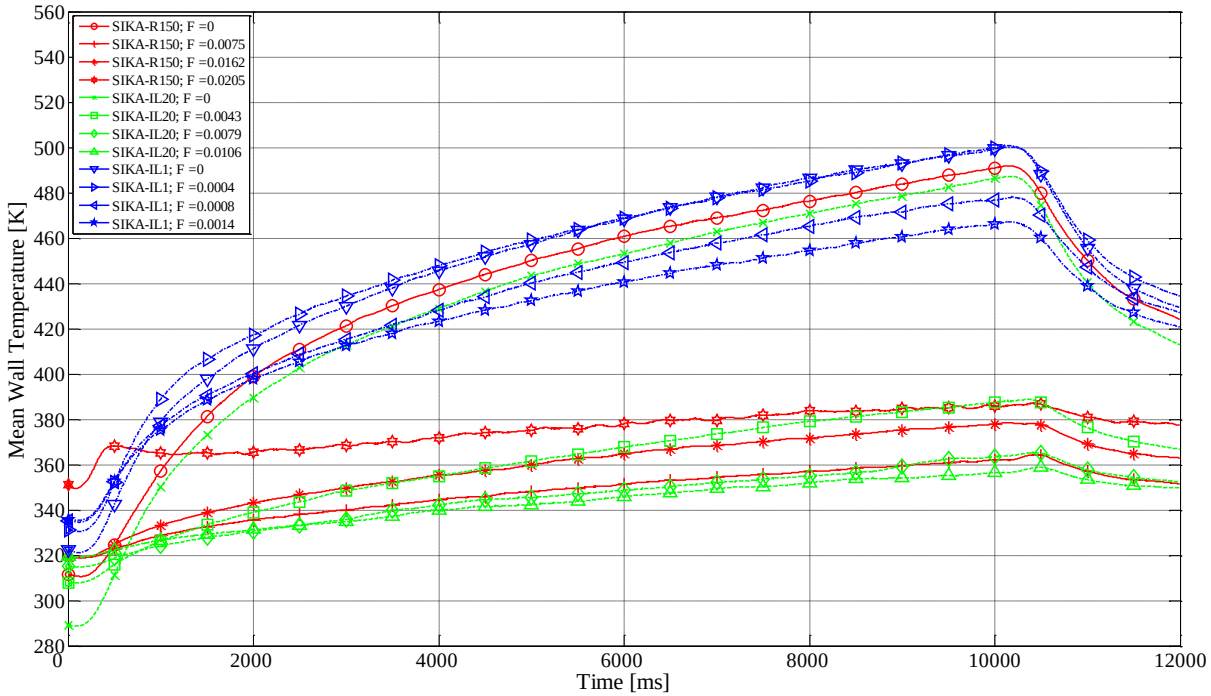

Figure 8: Mean Wall Temperature, 1200 K, 10 bar, Hydrogen, Shock Generator Position 112 mm

DOI: 10.13009/EUCASS2019-516

At those blowing ratios the oblique shock detaches from the shock generator (pre-choking state) which increases the development of a shock train. The fully developed shock train then switches back to a normal flow pattern after around 3 s. This decreases the mixing of hot gas from the main flow with the coolant boundary layer and thus reduces the resulting wall temperature. If the blowing ratio is increased further the shock train stays stable from the ignition of the air vitiator on, which corresponds to the higher mean wall temperatures in case of F=0.58 % and F=0.93 %.
If the blowing ratio is increased to 1.19 %, the shock train gets pushed further upstream and starts to choke the channel. The resulting flow pattern is a strongly fluctuating flow, which shifts between choking, pre-choking and a normal flow pattern back and forth.
Figure 8 compares the mean wall temperature distribution for 1200 K, 10 bar stagnation values, and a shock generator position of 112 mm. This particular boundary condition is especially prone to shock-boundary layer interaction (SBLI) induced auto-ignition of the hydrogen coolant. The cause for this sensitivity can be found in the frequent development of a shock train system that mixes oxidizer from the hot vitiated air into the hydrogen coolant boundary layer. This increased mixing can reach the boundary conditions needed for self-ignition, which is obvious in the wall temperature rise in the first 0.5 to 1.0 s in Fig. 8 at a blowing ratio of 2.05 %. After hydrogen ignition the flame gets ripped off the porous wall area and leaves the channel due to a lack of suitable flame holders in that area. Caused by the development of high mixing shock trains at higher blowing ratios, an increase of the blowing ratio beyond 1.06 %, leads to a rise of the mean wall temperature. Furthermore the lowest mean wall temperature reached under semi-steady state conditions is 360 K and therefore 20 K higher than in the 900 K, 15 bar case. The high initial temperatures are caused by residual heat in the air vitiator system after successive testing, which further increase the probability of a SBLI triggered self-ignition.

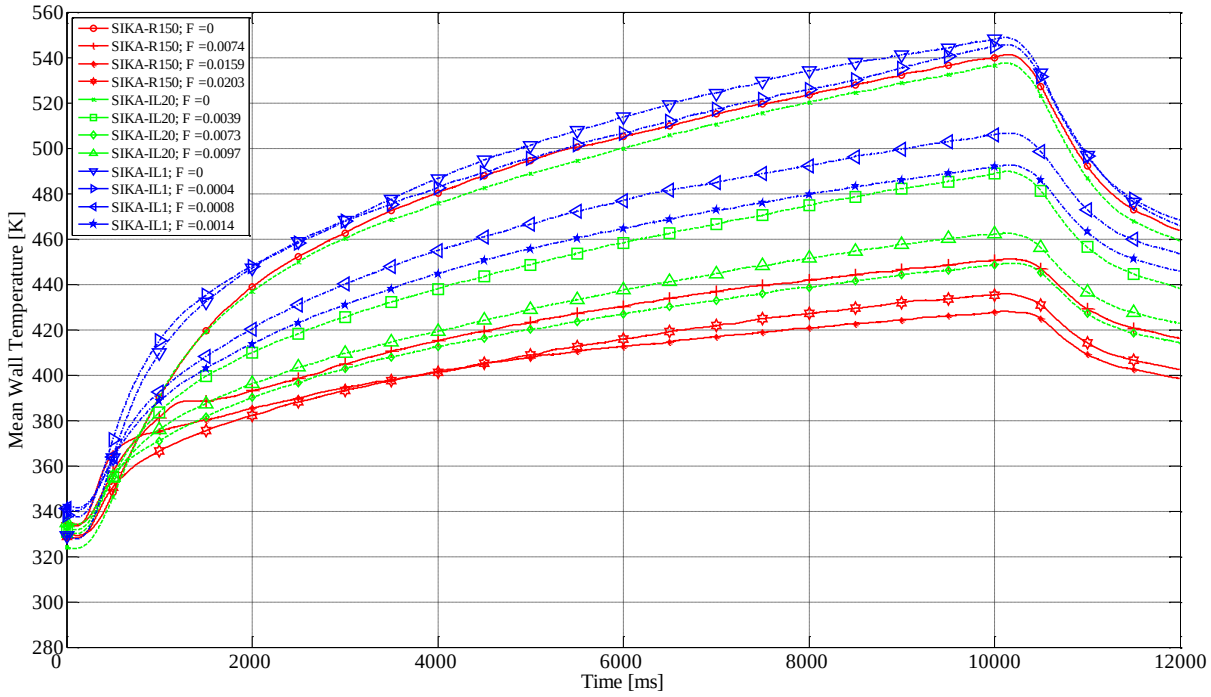

Figure 9: Mean Wall Temperature, 1200 K, 10 bar, Hydrogen, Shock Generator Position 177 mm

If the shock generator is moved downstream to the 177 mm position (refer to Fig. 9), the SBLI triggered self-ignition occurs at two boundary conditions: 0.74 % and 1.59 % (Sika-R150) in the first second of the hot run. BOS analysis indicates that at both blowing ratios the flow develops as a shock train flow, which triggers auto-ignition and switches to a normal flow pattern after ignition. The minimum mean wall temperature under semi steady-state conditions in Fig. 9 can be determined to 425 K, which is 65 K higher than at the 112 mm position in Fig. 8.

DOI: 10.13009/EUCASS2019-516

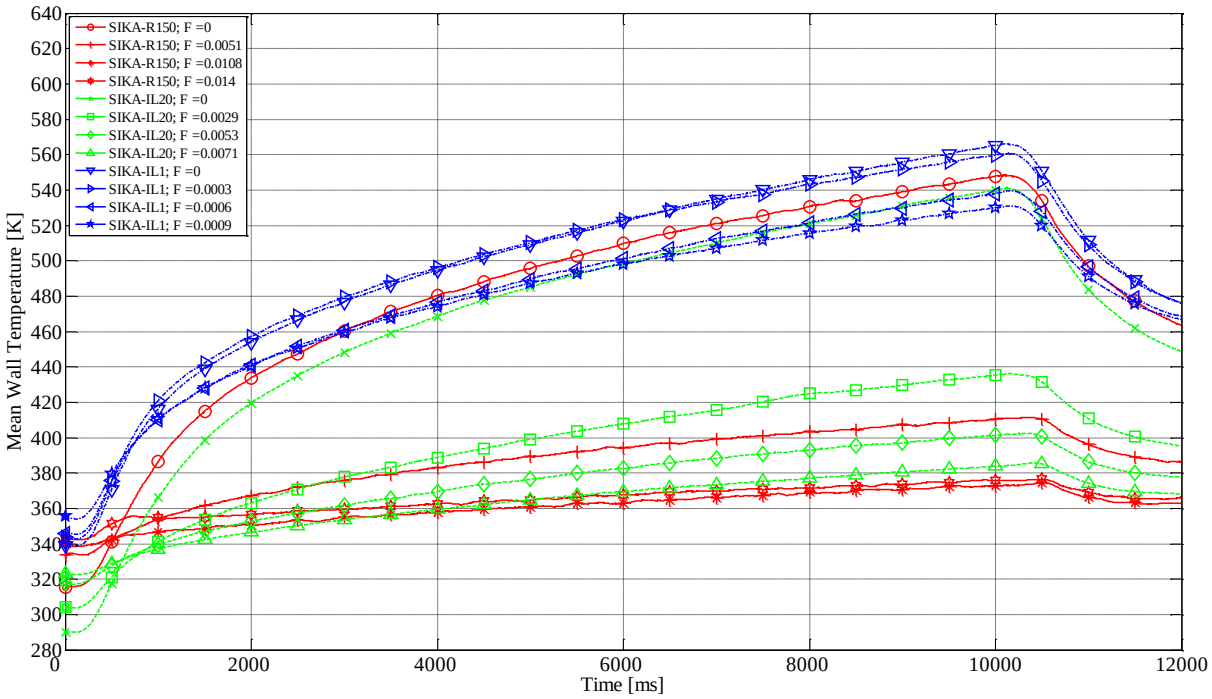

Figure 10: Mean Wall Temperature, 1200 K, 15 bar, Hydrogen, Shock Generator Position 112 mm

Figure 10 displays the mean wall temperature development for a 1200 K stagnation temperature, a 15 bar stagnation pressure, and a shock generator position at 112 mm. The maximum temperature reached in the uncooled case is 550 to 560 K compared to 500 K, in Fig. 8. The conditions for a shock train or a pre-self-ignition flow in Fig. 10 are reached at about 1 s test run time and 350 K mean wall temperature.

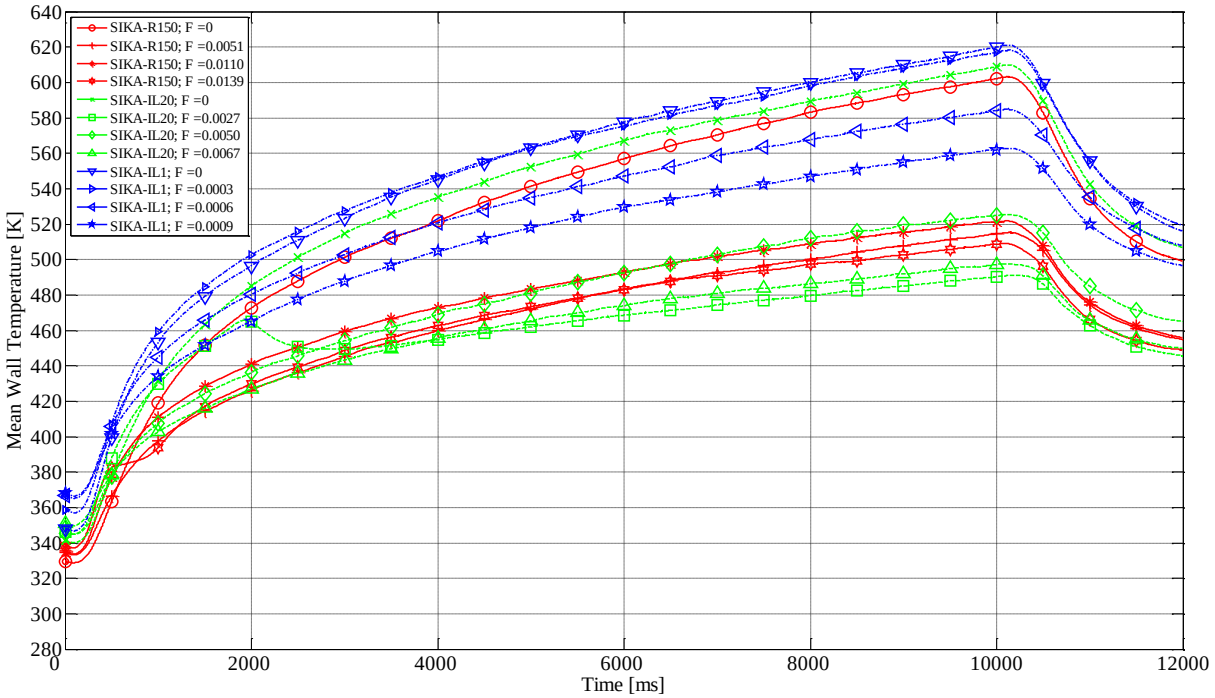

Figure 11: Mean Wall Temperature, 1200 K, 15 bar, Hydrogen, Shock Generator Position 177 mm

There the flow starts with a shock train system, which switches back to normal mode after about 1 s. Figure 10 is again a good example for the limited effectiveness of an increase in blowing ratio from a certain coolant mass flow rate on. Thus, an increase from 0.71 % (Sika-IL20) to 1.4 % (Sika-R150) reduces the mean wall temperature only for about 10 K. When the shock generator is positioned at 177 mm, the uncooled wall temperatures rise to a maximum of 620 K (refer to Fig. 11) and the temperatures with cooling to a minimum of 490 K at a blowing ratio of 0.27 %. At

DOI: 10.13009/EUCASS2019-516

this blowing ratio the flow build-up starts with a shock train close to choking conditions with an oblique shock wave detached from the shock generator's leading edge. This shock train switches at a run time of about 2 s to normal flow, which in turn reduces the heat load on the wall and results in a temperature drop of the mean wall temperature. The downstream position of the shock generator together with the thickened coolant boundary layer at this position blocks a larger part of the channel's cross section compared to the 112 mm position. This results in an earlier development of shock trains that increase the heating of the upper wall by an increased mixing with hot gas from the main flow. In Fig. 11 at a blowing ratio of 1.39 % this mixing results again in an auto-ignition of the coolant boundary layer in the first 0.5 to 1 s of the test run. Those self-ignition events can also suddenly choke the flow, especially in the 177 mm cases.

5.2 Cooling Efficiency Comparison

For the estimation of the cooling efficiency Θ (see Eq. (2)) based on the experimental data, T_w was determined from the mean value of the data obtained by the thermocouples "ST-01" to "ST-08" (see Fig. 2 for exact sensor positions). A decision filter mechanism in the data analysis prevents unwanted effects of single runaway values on the mean value. Thus, the data was smoothed by a Savitzky-Golay Filter and values with more than 97.5% of the local maximum value were used to decide the evaluation region. Afterwards, the unfiltered data was used to obtain the mean wall temperature. The coolant temperature T_c was obtained by the thermocouple in the supply plenum; whereas the nozzle exit temperature T_e was calculated out of the measured flow data of the air vitiator (see reference [36] on this calculation method). In order to calculate the recovery temperature at the nozzle exit $T_{r,e}$, the nozzle exit (see Eq. (3)) Mach number Ma_e and the recovery factor $r_{turb,e}$ are needed. The recovery factor $r_{turb,e}$ was calculated out of the Prandtl number at the nozzle exit Pr_e using the correlation for a turbulent boundary layer (see Eq. (4)).

$$\Theta = \frac{T_{r,e} - T_w}{T_{r,e} - T_c} \tag{2}$$

$$T_{r,e} = T_e\left(1 + r_{turb,e}\frac{(\kappa - 1)}{2}Ma_e^{\,2}\right) \tag{3}$$

$$r_{turb,e} = \left(\mathrm{Pr}_e\right)^{1/3} \tag{4}$$

Figure 12 shows the distribution of cooling efficiencies for the two different shock generator positions with respect to their blowing ratios for hydrogen. The cooling efficiency is displayed only in relative and not absolute numbers. The reason for this is an effect, which was first described by the authors in [33] and [34]: after some test runs on a single testing day, the entering hydrogen coolant becomes warmer than the wall temperature due to heat transfer between the warmed plenum structure and the coolant, even at a short residence time in the plenum. This leads to a negative or strongly over-predicted cooling efficiency according to Eq. (2). Therefore the authors decided to publish relative cooling efficiencies to show the influence of the shock generator and its position. In Fig. 12 the differences between the cooling efficiencies for the 112 mm and 177 mm cases are about 0 to 5 % for small blowing ratios (below 0.25 %; Sika-IL1) and 15 to 20 % for higher blowing ratios (above 0.25 %; Sika-IL20 and Sika-R150). The cause for this could be found in the steepening of the cooling boundary layer oblique shock angle at higher blowing ratios. A steeper shock would be reflected more upstream and therefore the reflected shock impinges on the coolant boundary layer earlier, which in turn additionally impairs the coolant boundary layer. Furthermore, the oblique shock generated by the shock generator impinges in the 177 mm case the coolant boundary layer on a position where it is thicker and therefore more sensitive to SBLI issues like boundary layer separation.

DOI: 10.13009/EUCASS2019-516

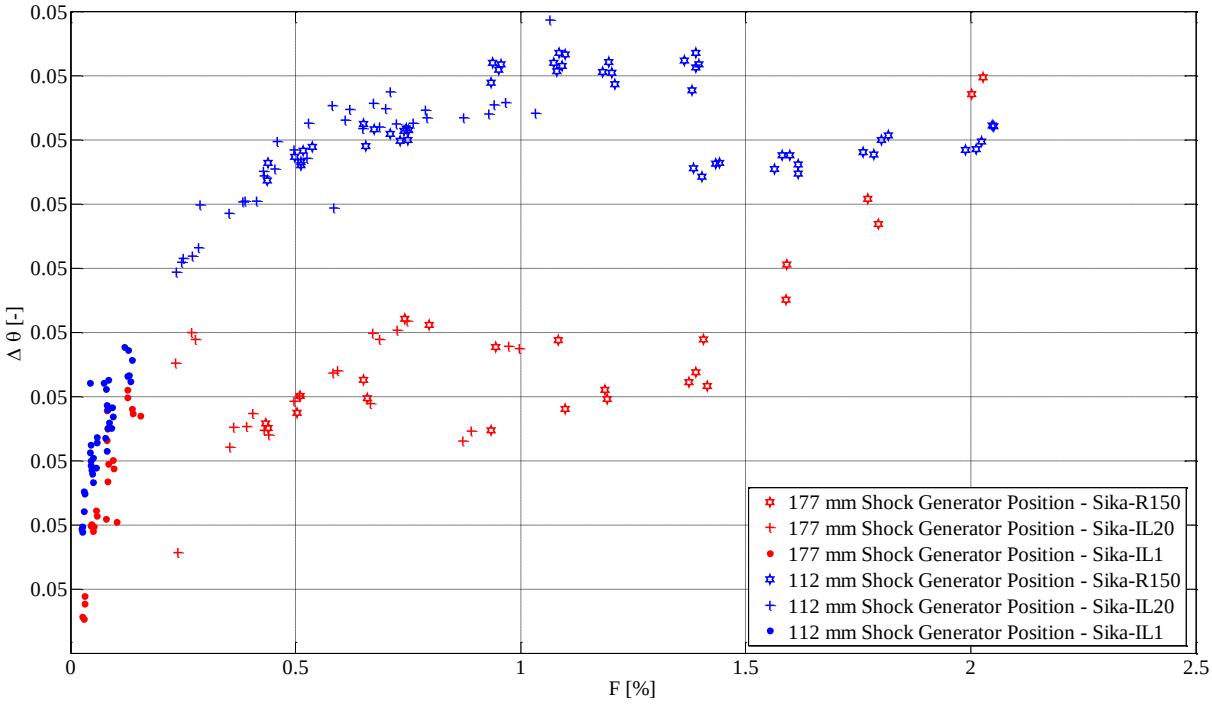

Figure 12: Influence of Shock Generator Position and Blowing Ratio on Cooling Efficiency for Hydrogen

6. Uncertainty Analysis

For every test run the random uncertainty of the mean $P_{\bar{x}}$ was calculated for the thermocouples after Eq. (5) (see [39]). In Eq. 4 S_x indicates the standard deviation and n is the number of measurements used for determining the average.

$$P_{\bar{x}} = 2\frac{S_x}{n^{0.5}} \tag{5}$$

For Fig. 4 and Fig. 5 the worst case value for $P_{\bar{x}}$ was 1.60 K, for Fig. 6 and Fig. 7 1.83 K, for Fig. 8 and Fig. 9 2.22 K and for Fig. 10 and Fig. 11 2.50 K. Assuming a systematic uncertainty of the thermocouples of (0.0075*measured temperature value) according to the manufacturer, the maximum total uncertainties are calculated to 3.38 K for Fig. 4 and Fig. 5, 3.83 K for Fig. 6 and Fig. 7, 4.13 K for Fig. 8 and Fig. 9 and 4.69 K for Fig. 10 and Fig. 11.
The coolant temperature T_c is as a worst case assumed to have a similar uncertainty, since it is measured by one single type K thermocouple. The nozzle exit temperature T_e is calculated via the stagnation temperature T_t. The stagnation pressure is determined via the pressure measurement and the velocity calculation in the air vitiator. The highest random uncertainty of the mean value in the pressure measurement was 0.064 bar for 15 bar stagnation pressure and 0.042 bar for 10 bar stagnation pressure. This causes a calculation uncertainty of about 0.4% or 2.2 K of T_e in the worst case. In summary the uncertainty of the cooling efficiency caused by measurement uncertainties is determined to below 2%.

7. Conclusion

DLR Lampoldshausen has conducted experiments on the applicability of transpiration cooling systems in supersonic combustion ramjets. In the publication at hand experimental results of gaseous hydrogen as coolant together with tree different porous wall materials made of sintered stainless steel and two different positions of a wedge shaped shock generator are compared. Results were presented for 96 different blowing ratios. The results presented show that the lateral position of a wedge shaped shock generator has a strong influence on the cooling efficiency in general and on the wall temperature distribution in particular. The phenomenon of SBLI induced self-ignition of the coolant could be observed at both shock generator positions. In general SBLI induced auto-ignition was observed more frequently and under different boundary conditions at the downstream position of the shock generator, compared to the upstream position. This is caused by a thicker boundary layer at the downstream position which causes earlier a pre-

choking or shock train flow condition. Those shock trains improve the mixing of hot gas as an oxidiser into the hydrogen coolant boundary layer until self-ignition conditions are reached. Furthermore it was found that the downstream position of the shock generator is more prone to instable or fluctuating flow behaviour. Findings from previous publications by the authors could be further confirmed, e.g. the increase of the wall temperature by very low blowing ratios and a kind of "saturation" effect, were an increase in blowing ratio causes only a minor decrease of mean wall temperatures.

8. Outlook

Additional experiments using CMC fibre reinforced ceramics of different thicknesses have been performed using nitrogen and hydrogen as coolant and different shock generator positions. The results of those experiments will be part of future publications by the authors. Results of test with extended test run time and its effect on the temperature and pressure distribution in the test setup will be addressed by future publications. Improvements to existing theoretical cooling models are developed at the moment in order to better depict the situation of a temperature measurement in the coolant wake region. The improvements also include a solution for the negative cooling efficiency issue with pre-heated coolant under realistic conditions.

Acknowledgements

The authors want to thank the staff of test bench M11 at the site of Lampoldshausen, especially Patrick Cragg, Lukas Werling, Hagen Friedrich, Jan Buddenberg and Marius Wilhelm for their outstanding support during the measurement campaign.

References

[1] Sholto, F., Smart, M. K., Kearney, M. P. and I. Jahn. 2018. Flyback of the SPARTAN Scramjet-Powered Launch Vehicle. 2018 AIAA Aerospace Science Meeting, Kissimmee, FL, AIAA 2018-2177. DOI: 10.2514/6.2018-2177.

[2] Rhoby, M., Okhovat, S., Kerst, A., Gross, K., and T. Ombrello. 2017. Preliminary Investigation of Scramjet Fueling Flowfield with Hyperspectral Imaging, 53rd AIAA/SAE/ASEE Joint Propulsion Conference, AIAA Propulsion and Energy Forum, Atlanta, GA, AIAA 2017-4646. DOI: 10.2514/6.2017-4646.

[3] Speier, R., Nacouzi, G., Lee, C. and R. Moore. 2017. Hypersonic Missile Nonproliferation - Hindering the Spread of a New Class of Weapons. RAND Corporation. RR-2237-CC. DOI: 10.7249/RR2137.

[4] Button, K. 2018. Hypersonic Weapons Race, in Aerospace America (Issue June 2018), AIAA– American Institute of Aeronautics and Astronautics, accessed June 7, 2019, from https://aerospaceamerica.aiaa.org/features/hypersonic-weapons-race/.

[5] Langener, T. 2011. A Contribution to Transpiration Cooling for Aerospace Applications Using CMC Walls. PhD Thesis. University of Stuttgart, Germany, Faculty of Aerospace Engineering and Geodesy.

[6] Greuel, D. 2013. Investigations on Momentum and Mass Transport in Effusion Cooled Rocket Combustion Chambers Made of Fibre Ceramics. PhD Thesis, RWTH Aachen, Germany.

[7] Babinsky, H. and J. K. Harvey. 2011. *Shock Wave-Boundary-Layer Interactions*. 1st ed., New York: Cambridge University Press, pp. 296-300.

[8] Serbest, E. 2001. Investigations on Application of Effusion Cooling in Rocket Combustion Chambers. PhD Thesis, RWTH Aachen, Germany.

[9] Capra, B. R., Boyce, R. R., Kuhn, M. and H. Hald. 2015. Combustion Enhancement in a Scramjet Engine Using Oxygen Enrichment and Porous Fuel Injection. *Journal of Fluid Mechanics*, Vol. 767 :173-198. DOI: 10.1017/jfm.2015.43

[10] Zierep, J., Bohning, R. and P. Doerffer. 2002. Perforated Plate Aerodynamics for Passive Shock Control. In: *IUTAM Symposium Transsonicum IV, Proceedings of the IUTAM Symposium*, Göttingen, Germany, September 2-6, 2002, pp. 125-130.

[11] Gascoin, N., Fau, G., Gillard, P., Kuhn, M., Bouchez, M. and J. Steelant. 2011. Benchmark of Experimental Determination Methods of Gas Permeabilities, 17th AIAA International Space Planes and Hypersonic Systems and Technologies Conference, San Francisco, CA. AIAA 2011-2252, 2011. DOI: 10.2514/6.2011-2252.

[12] Gascoin, N., Gillard, P., Bernard, S., Abraham, G., Bouchez, M., Daniau, E. and Y. Toure. 2006. Measurements for Fuel Reforming for Scramjet Thermal Management and Combustion Optimization: Status of the COMPARER Project, 14th AIAA/AHI Space Planes and Hypersonic Systems and Technology Conference, Canberra, AUS, AIAA 2006-8005, 2006. DOI: 10.2514/6.2010-6551.

[13] Gascoin, N., Fau, G., Bioud, J. and P. Gillard. 2010. Permeation of Inert and Supercritical Reactive Fluids Through Metallic and Composite Media, 48th AIAA/ASME/SEA/ASEE Joint Propulsion Conference and Exhibit, Nashville, TN. AIAA 2010-6551, 2010. DOI: 10.2514/6.2006-8005.

[14] Gascoin, N. and P. Gillard. 2011. Supersonic Combustion of Hydrocarbon Pyrolysed Coolant with Detailed Chemistry. 41st AIAA Fluid Dynamics Conference and Exhibit, Honolulu, HI, AIAA 2011-3712, 2011. DOI: 10.2514/6.2011-3712.

[15] Najmi, H., Tabach, E., Chetehouna, K., Gascoin, N. and F. Falempin. 2015. Effect of Flow Configuration on Darcian and Forchheimer Permeabilities Determination in a Porous Composite Tube, 20th AIAA International Space Planes and Hypersonic Systems and Technology Conference, Glasgow, UK. AIAA 2015-3665, DOI: 10.2514/6.2015-3665.

[16] Taddeo, L., Gascoin, N., Fedioun, I., Chetehouna, K., Lamoot, L. and G. Fau. 2015. High-End Experiments on Regenerative Cooling: Test Bench Design, 20th AIAA International Space Planes and Hypersonic Systems and Technologies Conference, Glasgow, UK. AIAA 2015-3664, 2015. DOI: 10.2514/6.2015-3664.

[17] Prokein, D., von Wolfersdorf, J., Dittert, Ch. and H. Börk. 2018. Transpiration Cooling Experiments on a CMC Wall Segment in a Supersonic Hot Gas Channel. International Energy Conversion Engineering Converence, AIAA Propulsion and Energy Forum, Cincinatti, OH, AIAA 2018-4696. DOI: 10.2514/6.2018-4696

[18] Prokein, D. and J. von Wolfersdorf. 2019. Numerical Simulation of Turbulent Boundary Layers with Foreign Gas Transpiration Using OpenFOAM. *Acta Astronautica*, Vol. 158 :253-263.

[19] Huang, Z., Zhu, Y., Xiong, Y. and P. Jiang. 2014. Investigation of Transpiration Cooling for Sintered Metal Porous Struts in Supersonic Flow. *Applied Thermal Engineering*, Vol. 70:240-249.

[20] Jiang, P., Huang, G., Zhu, Y., Liao, Z. and Z. Huang. 2017. Experimental Investigation of Combined Transpiration and Film Cooling for Sintered Metal Porous Struts. *International Journal of Heat and Mass Transfer*. Vol. 108:232-243. DOI: 10.1016/j.ijheatmasstransfer.2016.12.014.

[21] Holden, M., Nowak, R., Olsen, G. and K. Rodriguez. 1990. Experimental Studies of Shock Wave / Wall Jet Interaction in Hypersonic Flow. 28th AIAA Aerospace Science Meeting, Reno, NV. AIAA 90-0607, DOI: 10.2514/6.1990-607.

[22] Holden, M. S. and S. J. Sweet. 1994. Studies of Transpiration Cooling with Interaction in Hypersonic Flow. 25th Plasmadynamics Conference, Colorado Springs, CO. AIAA 94-2475. DOI: 10.2514/6.1994-2475.

[23] Olsen, G. C. and R. J. Nowak. 1995. Hydrogen Film Cooling With Incident and Swept-Shock Interactions in a Mach 6.4 Nitrogen Free Stream, National Aeronautics and Space Administration, NASA Technical Memorandum 4603.

[24] Meinert, J. 2000. Static Friction and Heat Transfer in a Turbulent Boundary Layer During Foreign Gas Transpiration. PhD Thesis. University of Dresden, Germany.

[25] Song, K., Choi, S. and S. Scotti. 2006. Transpiration Cooling Experiment for Scramjet Engine Combustion Chamber by High Heat Fluxes. *Journal of Propulsion and Power*, 22 (1):96-102. DOI: 10.2514/1.11300.

[26] Liu, Y., Jiang, P., Xiong, Y. and Y. Wang. 2013. Experimental and Numerical Investigation of Transpiration Cooling for Sintered Porous Flat Plates. *Applied Thermal Engineering*. Vol. 50:997-1007. DOI: 10.1016/j.applthermaleng.2012.08.028.

[27] Huang, G., Zhu, Y., Liao, Z., Ouyang, X. and P. Jiang. 2017. Experimental Investigation of Transpiration Cooling With Phase Change for Sintered Porous Plates. *International Journal of Heat and Mass Transfer* Vol. 114:1201-1213. DOI: 10.1016/j.ijheatmasstransfer.2017.05.114.

[28] Olsen, G., Holden, M. and Baker, M., (1990) Experimental Results for Film Cooling in 2-D Supersonic Flow Including Coolant Delivery Pressure, Geometry and Incident Shock Effects, 28th AIAA Aerospace Science Meeting, Reno, NV, AIAA 90-605. DOI: 10.2514/6.1990-605

[29] Alzner, E. and V. Zakkay. 1970. Turbulent Boundary Layer Shock Interaction with and without Injection, 8th AIAA Aerospace Science Meeting, West-Germany, AIAA 70-91. DOI: 10.2514/6.1970-91.

[30] Bernicker, P. 1961. Downstream Effects of Transpiration Cooling. *Journal of the Aerospace Sciences.* Vol. 28(8):658-659. DOI: 10.2514/8.9122.

[31] Strauss, F., Woessner, M., Weisswange, M., Manfletti, C. and S. Schlechtriem. 2017. Experiments on Flow Interaction in a Transpiration Cooled Model Scramjet, 7th European Conference of Aeronautics and Space Sciences (EUCASS). July 3rd–6th, 2017, Milan, Italy. EUCASS 2017-235. DOI: 10.13009/EUCASS2017-235.

[32] Strauss, F., Witte, J., Weisswange, M., Manfletti, C. and S. Schlechtriem. 2017. Experiments on Shock-Boundary Layer Interaction and Cooling Efficiency in a Transpiration Cooled Model Scramjet. 53rd AIAA/SAE/ASEE Joint Propulsion Conference, Atlanta, GA. AIAA 2017-4833. DOI: 10.2514/6.2017-4833.

[33] Strauss, F., Witte, J., Manfletti, C., and S. Schlechtriem. 2018. Experiments on Nitrogen and Hydrogen Transpiration Cooling in Supersonic Combustion Ramjets (Scramjets). 6th Space Propulsion Conference, 14th to 18th May 2018, Seville, Spain.

DOI: 10.13009/EUCASS2019-516

[34] Strauss, F., Witte, J, General, S., Manfletti, C., and S. Schlechtriem. 2018. Experiments on Nitrogen and Hydrogen Transpiration Cooling in a Model Scramjet Combustor. Joint Propulsion Conference, AIAA Propulsion and Energy Forum, Cincinatti, OH. AIAA 2018-4932. DOI: 10.2514/6.2018-4932.
[35] Kirchhartz, R. M. 2009. Upstream Wall Layer Effects on Drag Reduction with Boundary Layer Combustion, PhD Thesis, University of Queensland (UQ), Brisbane, Australia.
[36] Strauss, F., Manfletti, C., Lieberwirth, R. and S. Schlechtriem. 2016. Experimental Setup on Transpiration Cooling in Supersonic Combustion Ramjets (Scramjets). 5th Space Propulsion Conference, 2nd to 6th May 2016, Rome, Italy.
[37] Settles, G. S. 2001. *Schlieren and Shadowgraph Techniques*, 1st ed., New York: Springer-Verlag, pp. 39-48.
[38] Settles, G. S., and M. Hargather. 2017. A Review of Recent Developments in Schlieren and Shadowgraph Techniques. *Measurement Science and Technology*. 28, 042001. DOI:10.1088/1361-6501/aa5748.
[39] Wheeler, J. and A. Ganji. 2010. *Introduction to Engineering Experimentation*. 3rd Edition. Pearson. pp.206-207.